The Astrophysical Journal, 797:51 (7pp), 2014 December 10 doi:10.1088/0004-637X/797/1/51

RADIAL DISTRIBUTION OF COMPRESSIVE WAVES IN THE SOLAR CORONA REVEALED BY *AKATSUKI* RADIO OCCULTATION OBSERVATIONS

Mayu Miyamoto[1], Takeshi Imamura[2], Munetoshi Tokumaru[3], Hiroki Ando[2], Hiroaki Isobe[4], Ayumi Asai[4], Daikou Shiota[3], Tomoaki Toda[2], Bernd Häusler[5], Martin Pätzold[6], Alexander Nabatov[7], and Masato Nakamura[2]
[1] Department of Earth and Planetary Science, The University of Tokyo, 7-3-1 Hongo, Bunkyo-ku, Tokyo 113-0033, Japan
[2] Institute of Space and Astronautical Science, Japan Aerospace Exploration Agency, 3-1-1, Yoshinodai, Chuo-ku, Sagamihara, Kanagawa 252-5210, Japan
[3] Solar-Terrestrial Environment Laboratory, Nagoya University, Furo-cho, Chikusa-ku, Nagoya, Aichi 484-8601, Japan
[4] Unit of Synergetic Studies for Space, Kyoto University, Yamashina, Kyoto 607-8471, Japan
[5] Institut für Raumfahrttechnik, Universität der Bundeswehr München, D-85577 Neubiberg, Germany
[6] Rheinisches Institut für Umweltforschung, Department Planetenforschung, Universität zu Köln, Aachener Str. 209, D-50931 Köln, Germany
[7] The Institute of Radio Astronomy, National Academy of Science of Ukraine, Chervonoprapornaya, Str. 4, Kharkov 61002, Ukraine
Received 2014 April 16; accepted 2014 October 21; published 2014 November 25

ABSTRACT

Radial variations of the amplitude and the energy flux of compressive waves in the solar corona were explored for the first time using a spacecraft radio occultation technique. By applying wavelet analysis to the frequency time series taken at heliocentric distances of 1.5–20.5 R_S (solar radii), quasi-periodic density disturbances were detected at almost all distances. The period ranges from 100 to 2000 s. The amplitude of the fractional density fluctuation increases with distance and reaches ∼30% around 5 R_S, implying that nonlinearity of the wave field is potentially important. We further estimate the wave energy flux on the assumption that the observed periodical fluctuations are manifestations of acoustic waves. The energy flux increases with distance below ∼6 R_S and seems to saturate above this height, suggesting that the acoustic waves do not propagate from the low corona but are generated in the extended corona, probably through nonlinear dissipation of Alfvén waves. The compressive waves should eventually dissipate through shock generation to heat the corona.

Key words: solar wind – Sun: corona – waves

Online-only material: color figures

1. INTRODUCTION

The mechanism by which the solar corona is heated to a temperature of 10^6 K and accelerated to supersonic speeds is still unclear. Energy needs to be deposited both close to the solar surface to produce the sharp transition region and at a large range of distances in the extended corona beyond several R_S (R_S = solar radii) to accelerate high-speed streams (e.g., Cranmer 2002). Alfvén waves are believed to play an important role for coronal heating because they are transverse waves and thus can travel a long distance before dissipation. In fact, Alfvén waves have been detected in coronagraph images in the vicinity of the Sun including chromospheric bright points (Jess et al. 2009), spicules (De Pontieu et al. 2007), the chromosphere to the coronal base (McIntosh et al. 2011), solar prominences (Okamoto et al. 2007), and the lower corona (Tomczyk et al. 2007). These waves are generally thought to be generated by convection-driven jostling of magnetic flux tubes in the photosphere. Wave generation by nanoflares is another possibility (Isobe et al. 2008). Acoustic (slow magneto-acoustic) waves propagating from the photosphere to the chromosphere and the low corona have also been observed in coronagraph images (Ofman et al. 1997, 1999, 2000; De Forest & Gurman 1998; Carlsson et al. 2007; Gupta et al. 2012). Acoustic waves are also expected to heat the lower corona, although they will not propagate to the extended corona because of shock dissipation in the stratified atmosphere (Ofman et al. 2000).

Waves in the extended corona are much less understood because of the difficulty in observations. Observations of Faraday rotation in radio occultation signals of the *Helios* and *Messenger* spacecraft suggested periodical oscillations of the coronal magnetic field at 1.6–12 R_S, which are attributed to Alfvén waves (Hollweg et al. 1982; Chashei et al. 1999; Efimov et al. 2013a; Jensen et al. 2013). The Alfvén waves are considered to be in a regime of free propagation based on the radial dependence of the Faraday rotation fluctuations (Andreev et al. 1997). Compressive waves with periods of 1–80 minutes were observed at 3–40 R_S as quasi-periodic components (QPCs) of the frequency fluctuation of the radio signals of the *Ulysses*, *Galileo*, *Mars Express*, *Venus Express*, and *Rosetta* spacecraft (Efimov et al. 2010, 2012, 2013b). The frequency fluctuation reflects variations in the column-integrated electron density as described later. Efimov et al. (2012) attributed the observed compressive waves to acoustic waves generated locally via nonlinear interactions of Alfvén waves based on a theoretical expectation that acoustic waves generated in the photosphere cannot propagate far beyond the low corona. Despite these observations, the radial variations of the wave amplitude and the associated energy flux are not constrained.

Suzuki & Inutsuka (2005) showed, using a one-dimensional MHD model, that the dissipation of Alfvén waves through the nonlinear generation of slow (acoustic) waves and shocks heats the plasma in coronal holes to create the supersonic flow. In their model, the energy flux of outgoing Alfvén waves drops at >2 R_S, while the energy flux of slow waves increases with distance and peaks around 3–20 R_S, where the slow waves become nonlinear and lead to shock dissipation. Matsumoto & Suzuki (2012) obtained a similar result using a 2.5 dimensional MHD model which includes the details of wave reflection from the transition region, nonlinear mode conversion and turbulent cascade, although the radial variation of the characteristics of slow waves is not provided. Cranmer (2010) argued, using a one-dimensional Alfvén wave reflection model, that turbulence driven by reflection of Alfvén waves in the corona leads to dissipation of wave energy to heat the corona. The resultant turbulent heating rate peaks around 2–10 R_S. These model studies imply that observations of compressive waves in this region can constrain the energy deposition by Alfvén waves because such compressive waves should be either acoustic waves generated directly by dissipating Alfvén waves through nonlinearity (Suzuki & Inutsuka 2005, 2006) or those generated by turbulence caused by breaking Alfvén waves (Cranmer 2010).

Based on such an interest in the possible key role of acoustic waves in the energy deposition in the corona, we explore the radial dependence of the characteristics of compressive waves at heliocentric distances from 1.5 to 20.5 R_S by radio occultation experiments using JAXA's *Akatsuki* spacecraft. An advantage of radio occultation compared to optical observations is that density fluctuations can be observed with high accuracy via frequency measurements over a large range of heliocentric distances. Wavelet analysis allows detection of nonstationary wave packets in the corona. In Section 2, we describe the observation system and geometry, data set, and the method of retrieving the frequency fluctuation. In Section 3, quasi-periodic events are identified by wavelet analysis. In Section 4, the radial dependences of the density amplitude and the wave energy flux are obtained. The conclusions are given in Section 5.

2. DATA SET

Radio occultation observations of the solar corona were conducted during 2011 June 6 to July 8 using the Japanese Venus explorer *Akatsuki* (Nakamura et al. 2011), which is planned to be inserted into Venus's orbit at the end of 2015 to explore the Venusian meteorology. The observation conditions are summarized in Table 1 and the geometry of the solar conjunction in the sky projection are illustrated in Figure 1. The former half of the period (June 6–25) covers the western side of the Sun, and the latter half (June 26–July 8) covers the eastern side. The experiment at 12.7 R_S (June 13) was influenced by a coronal mass ejection (CME) which occurred near the western limb of the Sun and thus this observation is excluded from the analysis. Studies of the CME focusing on its velocity and density structure are ongoing and will be presented elsewhere. The solar activity was in a rising phase during this period. According to simultaneous observations conducted during June 24–27 using the space solar telescope *Hinode* (Kosugi et al. 2007), prominent coronal holes did not exist, although localized open magnetic fields were seen in the northeast area. Potential magnetic field calculations from surface magnetic field maps (Shiota et al. 2012; Balasubramaniam & Pevtsov 2011) suggest that closed fields were dominant below the tangential points (closest approach of the radio ray path to the Sun). The solar wind synoptic map generated with interplanetary scintillation (IPS) measurements by the STEL of Nagoya University (Kojima & Kakinuma 1990) indicates that slow winds were predominant at the observed locations. Details of the observations are given in Imamura et al. (2014).

The measurements utilized the radio science subsystem of the *Akatsuki* spacecraft (Imamura et al. 2011). The experiments were conducted using the 8.4 GHz (*X*-band) downlink signal stabilized by an onboard ultrastable oscillator (USO) having an Allan deviation less than 10^{-12} at the integration time from 1 to 1000 s. The radio wave transmitted from the high-gain antenna on the spacecraft is received at the Usuda Deep Space Center

Table 1
Observation Conditions

2011 Date	Time (UT)	Length (hr)	R (R_S)	East/West	v_{sw} (km s^{-1})
June 6	01:30	3.0	20.5	West	366
June 10	01:56	5.0	16.0	West	323
June 13[a]	01:00	6.0	12.7	West	296
June 15	01:00	6.0	10.5	West	226
June 17	01:00	6.0	8.4	West	150
June 20	01:00	6.0	5.4	West	33
June 22	01:00	6.0	3.5	West	64
June 24	01:00	6.0	1.9	West	58
June 25[b]	00:00	7.5	1.5	West	190
June 26	00:00	7.5	1.7	East	75
June 27	01:00	6.0	2.4	East	27
June 29	01:00	6.0	4.0	East	34
July 1	01:00	6.0	5.8	East	77
July 4	01:00	6.0	8.6	East	94
July 5	01:00	5.0	9.5	East	156
July 8	01:17	4.7	12.2	East	272

Notes. "Time" is the start of recording signals, "Length" is the recording length in hours, R is the heliocentric distance in the middle of each observation, and v_{sw} is the radial velocity of the solar wind which is taken from the velocity measurements by radio scintillation technique during this period (Imamura et al. 2014).
[a] This observation was excluded because of the influence of a CME.
[b] Superior conjunction.

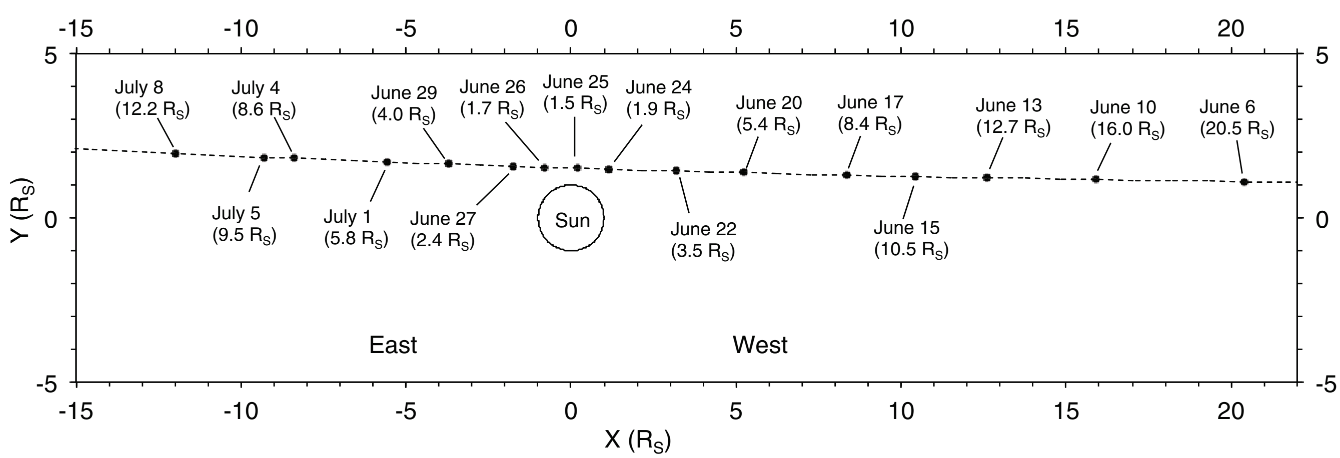

Figure 1. Locations of *Akatsuki* relative to the Sun as seen from the Earth in the heliocentric Cartesian coordinates during the experiment conducted in 2011. The y axis is directed to the north of the Sun.

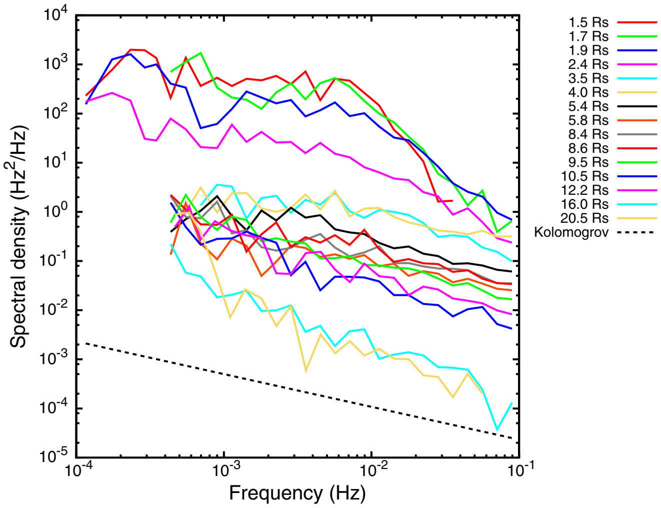

Figure 2. Power spectra of frequency fluctuation. Legends indicate heliocentric distances. The dashed line shows a power law with the spectral index of $-2/3$ (Kolmogorov).

(A color version of this figure is available in the online journal.)

(UDSC) of Japan, which has a 64 m dish antenna for deep-space communication. The received signals were down-converted to around 125 kHz by an open-loop heterodyne system stabilized by a hydrogen maser and 8 bits digitized with the sampling rate of 500 kHz.

The frequency fluctuation is retrieved from the recorded signal in the following manner (Imamura et al. 2005). First the frequency variation due to the radial velocity between spacecraft and ground station is subtracted from the original signal time series by heterodyning. In order to increase the signal-to-noise ratio, the bandwidth of the data is then reduced from 250 kHz to 1 kHz. This signal time series is divided into successive blocks with intervals of approximately 1 s, and a discrete Fourier transform (DFT) is applied to these blocks to obtain a frequency time series from the center frequencies of the signal spectra. The signal frequency is determined by two methods depending on the heliocentric distance: fitting a theoretical spectrum of a monochromatic radio wave (sinc function) to the DFT spectrum using a least squares method, or calculating the centroid of the signal spectrum. The former (fitting method) is appropriate for sufficiently narrow spectral lines, while the latter (centroid method) works better for spectral lines broadened by the turbulent medium. Based on a comparison of the noise levels from the two methods, we adopt the fitting method for $\geqslant 4\ R_S$ and the centroid method for $<4\ R_S$, although the two methods yield similar results.

The overall radial dependence of the power spectrum of the frequency time series is shown in Figure 2. The high-frequency portions ($>10^{-1}$ Hz) of the original spectra were dominated by white noise due to the frequency determination error and the oscillator noise, while the low-frequency portions ($<4 \times 10^{-4}$ Hz or $<10^{-4}$ Hz depending on the distance) were dominated by the oscillator noise with negative spectral slopes. The frequency ranges dominated by such background noise components have been removed in Figure 2. The power tends to increase with the decreasing heliocentric distance, being consistent with previous observations (Woo & Armstrong 1979; Imamura et al. 2005). Power-law dependence is evident over the frequency interval 10^{-3} Hz $< \nu < 10^{-1}$ Hz at 3.5–20.5 R_S, while bumps appear at 1.5–2.4 R_S. The spectral index of the power law is close to the Kolomogrov value of $-2/3$, suggesting an inertial subrange of fully developed turbulence. The bump feature seen at 1.5–2.4 R_S might indicate that the turbulence outer scale corresponds to this frequency range in this region. It is also possible that compressive waves contribute to this feature. Spangler (2002) studied the power-law phase fluctuations for very long baseline interferometers and shown that the fractional density amplitude of the solar wind turbulence is 6%–15% at 16–26 R_S. Compressive waves that we study are thought to be embedded in such background turbulence.

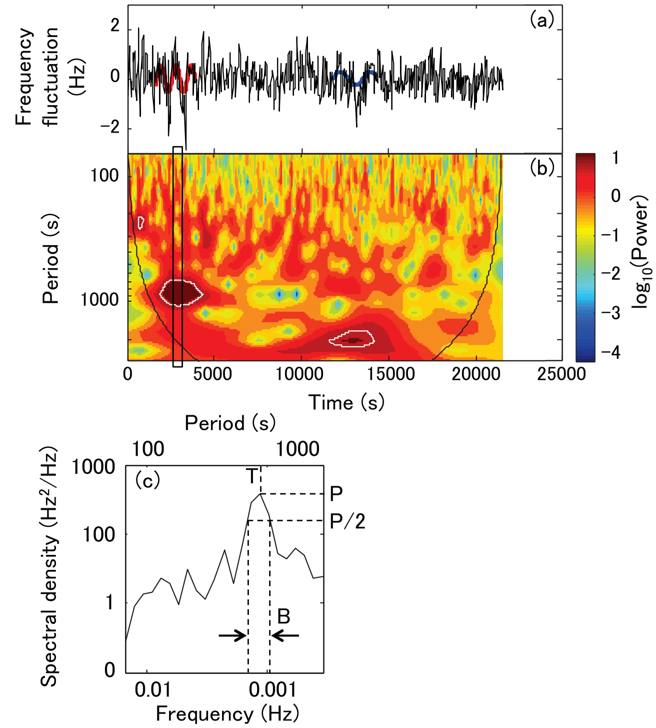

Figure 3. (a) Example of the signal frequency time series after bandpass filtering taken at 2.4 R_S. The red and blue lines are the sine functions corresponding to detected spectral peaks. (b) Wavelet power spectrum obtained from the time series given in (a). The spectrum was normalized so that the expectation value would be unity for a white-noise process. The regions under the black line indicate the COI where the edge effect is significant. White lines enclose regions where the statistical significance exceeds 95%. (c) Fourier spectrum averaged in the time interval indicated by a rectangular box in panel (b).

(A color version of this figure is available in the online journal.)

3. WAVELET ANALYSIS

Wavelet analysis is applied to the frequency time series to detect nonstationary periodical disturbances in the corona. We use a wavelet transform routine developed by Torrence & Compo (1998), which is based on the Morlet wavelet function and has been widely used in many geophysical and astronomical applications, with some modifications. The high-frequency noise described in the previous section was removed by averaging the data in every 30 s intervals, corresponding to a low-pass filter with a cutoff frequency (50% power reduction) of $\sim 1.7 \times 10^{-2}$ Hz. The low-frequency noise was removed by subtracting the moving average of the time series above with the window width of 1500 s from the time series without moving average. This corresponds to a high-pass filter with a cutoff frequency of $\sim 4.8 \times 10^{-4}$ Hz. An example of the frequency time series after bandpass filtering and the corresponding wavelet power spectrum are shown in Figure 3. The spectra have been normalized so that white noise would have an expectation value

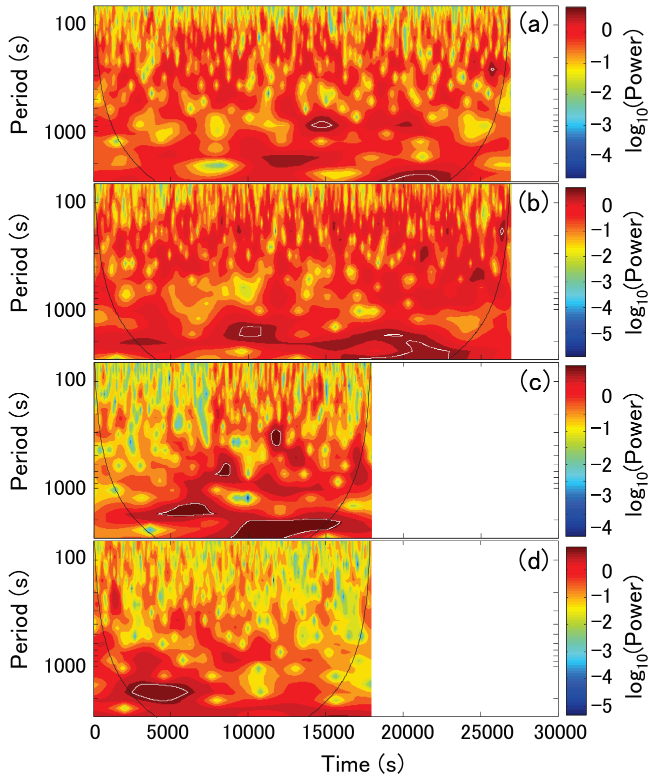

Figure 4. Wavelet power spectra of the frequency fluctuation at (a) 1.5, (b) 1.7, (c) 9.5, and (d) 16.0 R_S. The format of the plot is the same as that of Figure 3(b).

(A color version of this figure is available in the online journal.)

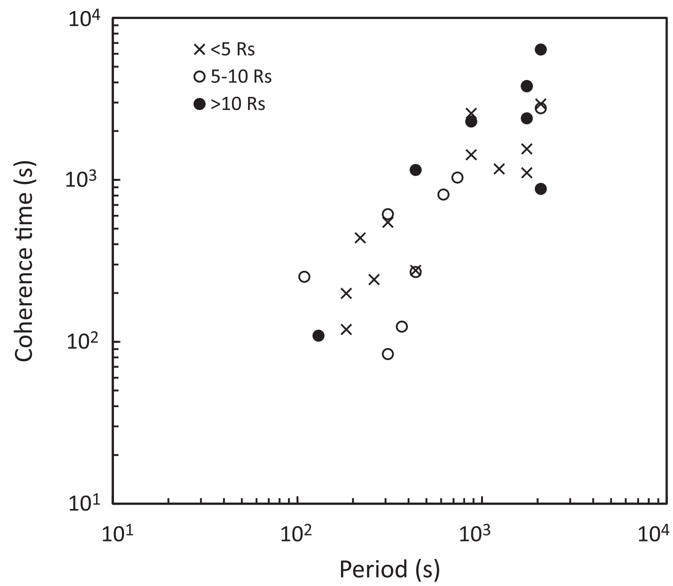

Figure 5. Relationship between the period and the coherence time for all quasi-periodic events at $<5\ R_S$ (crosses), 5–10 R_S (open circles) and $>10\ R_S$ (filled circles).

of unity at all frequencies in this plot and hereafter. The region of the wavelet spectrum where the effect of the discontinuity at the edge of the time series becomes significant is defined by the cone of influence (COI), whose boundaries are indicated by black curves in the spectra.

The statistical significance of spectral peaks is evaluated by randomization tests following the Fisher's method described by Nemec & Nemec (1985). The method gives an estimate of the probability that no periodic component is present in the data by comparing the maximum power peaks of a large number of random permutations of the time series data with the peak power of the original series. For example, the magnitudes $y_1, y_2, \ldots, y_n$, observed at $t_1, t_2, \ldots, t_n$, are just likely to have occurred in any other order $y_{r(1)}, y_{r(2)}, \ldots, y_{r(n)}$, where $r(1), r(2), \ldots, r(n)$ is a random permutation of the subscripts, $1, 2, \ldots, n$. By comparing the highest peak in the wavelet spectrum evaluated from the random order time series data, $P_{r\,\max}$, to the peak in the wavelet spectrum of the original ones, P, we can test the hypothesis that there is no periodicity in the data. Here, there are $n!$ equally likely permutations of the random order time series data. In practice, $n!$ is usually so large that it is impossible to calculate all of these because of computational time constraints, and thus the peak heights are generally calculated for only a random sample of m permutations.

The proportion of permutations that give peak heights greater or equal to the peak height of the original time series provides an estimate of the p value, the probability that no periodic component is present in the data. When m is sufficiently large ($m > 100$), the standard error of the estimated p value can be approximated by the formula $[p(1-p)/m]^{1/2}$, which has a maximum value of $0.5\,m^{-1/2}$. The probability levels for this work are the percentage probability levels that periodic components are present in the data, that is $(1-p) \times 100$. We chose a value of 95% as the lowest acceptable probability level. We calculated 200 ($= m$) permutations for a reliable estimate of p, giving the standard error of p value of no greater than $0.5 \times 200^{-1/2} \times 100 = 3.5\%$. The contours of 95% probability are indicated by white curves in the spectra. In the example shown in Figure 3, three peaks exceeding this probability level are identified.

Figure 4 shows four other examples of the wavelet spectra at 1.5, 1.7, 9.5, and 16.0 R_S. Quasi-periodic density fluctuations appear intermittently at various periods and all heliocentric distances except for 20.5 R_S, and the frequency of occurrence does not seem to depend noticeably on the distance. We identified 28 statistically significant peaks in total.

The relationship between the period and the coherence time, which is defined by the time interval where the statistical significance exceeds 95%, is shown for all quasi-periodic events in Figure 5. Both the period and the coherence time do not depend noticeably on the heliocentric distance. The periods are distributed over the range of 100–2000 s, which is consistent with the observations of QPCs at 3–40 R_S (Efimov et al. 2010, 2012, 2013b). The prevalence of oscillations having periods longer than several hundred seconds suggests that the waves do not originate in the photosphere but are generated in the corona, because acoustic waves having such periods cannot propagate through the transition region where the cut-off period drops to 150 s (Erdélyi et al. 2007). The coherence time generally has a value on the same order of magnitude as the wave period. If the coherence time is taken as the time which a wave packet takes to traverse the radio ray path, the result suggests that each wave packet contains only one or several oscillations.

4. WAVE AMPLITUDE AND ENERGY FLUX

The frequency deviation due to plasma, δf, is related to the time rate of change of the electron column density integrated along the ray path, dN/dt, as (e.g., Imamura et al. 2010):

$$\delta f = \frac{\alpha}{cf}\frac{dN}{dt}, \tag{1}$$

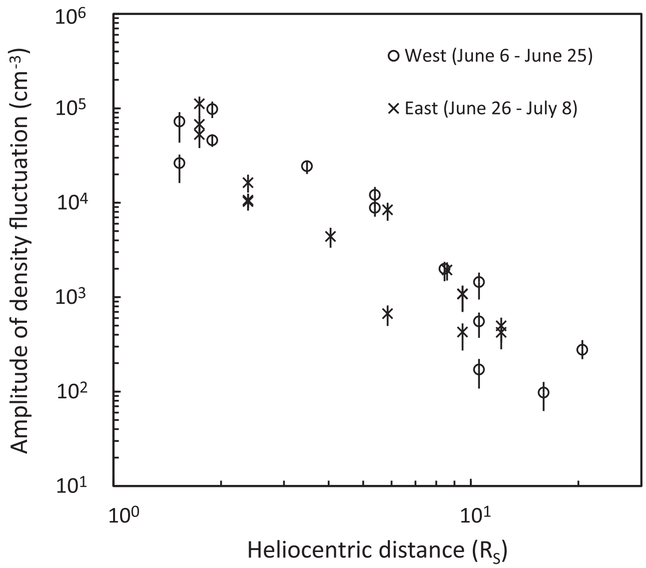

Figure 6. Density amplitude on the western side (circles) and the eastern side (crosses) of the Sun, with vertical bars indicating the error range.

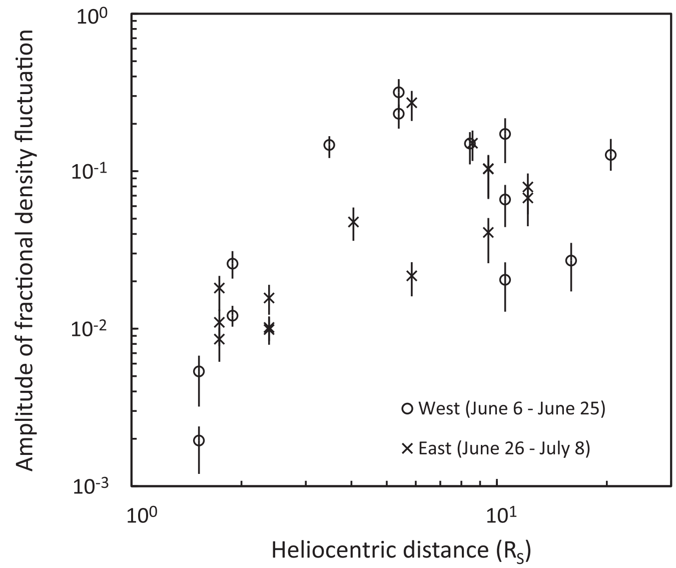

Figure 7. Amplitude of the fractional density fluctuation on the western side (circles) and the eastern side (crosses) of the Sun, with vertical bars indicating the error range.

where $\alpha = e^2/8\pi^2\varepsilon_0 m_e \sim 40.3$ m^3 s^{-2} with e, ε_0 and m_e being the elementary charge, dielectric constant in vacuum and electron mass, respectively, c the speed of right, and f the frequency of the radio wave. Here we assume the column density contains an oscillating component with a period T. Letting f' and N' be the amplitudes of the frequency and the column density, respectively, Equation (1) reduces to

$$f' = \frac{2\pi\alpha}{cfT}N'. \tag{2}$$

This relationship enables estimation of N' from the observed T and f'.

The procedure for determining f' is illustrated in Figure 3. First, the time interval which spans the spectral peak in the wavelet spectrum is chosen (Figure 3(b)). Second, the peak spectral density P, the FWHM B, and the period T of the spectral peak are obtained from the power spectrum averaged in this time interval (Figure 3(c)). Then, the amplitude of the frequency fluctuation is estimated by

$$f' = \sqrt{2PB}. \tag{3}$$

This procedure is repeated for all spectral peaks enclosed by white contours (95% statistical significance) observed in the wavelet spectra. The obtained T and f' well reproduce the oscillatory structures seen in the frequency time series (Figure 3(a)).

Conversion of the column density amplitude N' to the density amplitude n' requires a model of the spatial structure of the density fluctuation. We consider the length scale of the density fluctuation along the ray path is the same as the length of the wave packet. On the assumption that the waves are acoustic waves and that they propagate radially outward near the tangential point, this length is estimated by $T_{\mathrm{coh}}(v_{\mathrm{sw}} + c_s)$, where T_{coh} is the observed coherence time (Figure 5), v_{sw} is the radial velocity of the solar wind, and c_s is the sound speed. The validity and the influence of the assumption of outgoing waves will be discussed later. The phase velocity of slow waves matches the sound speed when the propagation direction is parallel to the magnetic field. Under this condition, n' is estimated by

$$n' = \frac{N'}{T_{\mathrm{coh}}(v_{\mathrm{sw}} + c_s)}. \tag{4}$$

Here $c_s \sim 160$ km s^{-1} for the 10^6 K corona, and v_{sw} is taken from the radio scintillation measurement of the outflow speed during the same period (Imamura et al. 2014) and given in Table 1. The v_{sw} is relatively small ($<$100 km s^{-1}) inside $\sim$5 R_S, increases rapidly with distance at 6–13 R_S, and approaches asymptotically to 400–500 km s^{-1} at farther distances.

By using Equations (2) and (4), the density amplitude n' is obtained from the observed T, T_{coh}, and f' as a function of the heliocentric distance as shown in Figure 6. The error bars take into account the uncertainties in T, B, P, and v_{sw}. The amplitude decreases with distance similarly on the western and eastern side of the Sun.

Here we assume that the radial dependence of the background electron density n_0 is represented by the empirical model proposed by Pätzold et al. (1987):

$$n_0(r) = \left(\frac{5.79}{r^{16}} + \frac{1.6}{r^6} + \frac{9.2 \times 10^{-3}}{r^2}\right) \times 10^8 \text{ cm}^{-3}, \tag{5}$$

where r is the heliocentric distance in unit of R_S. Then, the radial distribution of the fractional density amplitude n'/n_0 is obtained as shown in Figure 7. The fractional density amplitude increases with heliocentric distance at $<$5.4 R_S to reach a maximum value of $\sim$0.3, and keeps a roughly constant value or decreases at farther distances. The remarkable similarity between the western side and the eastern side suggests that this feature is not caused by temporal variation but reflects a spatial structure. The estimated amplitude implies that nonlinearity of the wave field is potentially important: nonlinear steepening of wave fronts and shock dissipation are expected to occur. This feature is roughly consistent with the result of the one-dimensional MHD model by Suzuki & Inutsuka (2005), who showed that outgoing Alfvén waves generate outgoing longitudinal slow waves, which eventually become nonlinear at $\sim$3 R_S to lead to shock dissipation and subsequent coronal heating. The

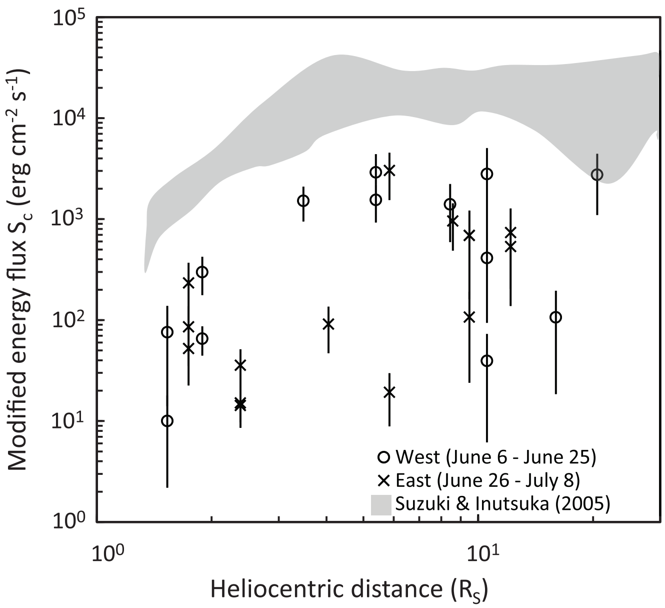

Figure 8. Modified energy flux S_c of acoustic waves obtained from the observations on the western side (circles) and the eastern side (crosses) of the Sun, with vertical bars indicating the error range. The S_c of slow waves in the numerical model by Suzuki & Inutsuka (2005) is also plotted for comparison (shades).

magnitude of the fractional density amplitude is within the same order of magnitude as the estimates from *Ulysses* ranging measurements at 4–20 R_S in the slow wind (Woo et al. 1995). Note, however, that our result cannot be compared directly with those estimates, because only quasi-monochromatic fluctuations are considered in our study, whereas the background turbulent fluctuation is considered in the *Ulysses* measurements.

Figure 8 shows the radial distribution of the modified energy flux S_c introduced by Jacques (1977) and Suzuki & Inutsuka (2005):

$$S_c = m_p n_0 v'^2 \frac{(v_{\rm sw} + c_s)^2}{c_s} \frac{r^2 g(r)}{r_c{}^2 g(r_c)}, \tag{6}$$

where m_p is the proton mass, v' is the velocity amplitude of the acoustic wave, which is estimated as $v' = c_s n'/n_0$, $g(r)$ is the function for superradial expansion (Kopp & Holzer 1976; Suzuki & Inutsuka 2005), and $r_c = 1.02\ R_S$ is the distance for normalization. The S_c is an adiabatic constant in the expanding atmosphere under the condition that no wave generation and dissipation occur. Since $g(r)$ takes into account a rapid expansion below $\sim$1.2 R_S and remains unity above $\sim$1.2 R_S, the choice of the superradial expansion factor does not influence the relative radial dependence of the result covering 1.5–20.5 R_S. The observed increase of S_c with distance at $<$6 R_S suggests that the acoustic waves do not originate from the low corona but are generated in the extended corona.

In Figure 8, the range of S_c for outgoing slow waves in the one-dimensional model by Suzuki & Inutsuka (2005) is also plotted for comparison. The overall radial variation is qualitatively similar between the observation and the model, suggesting a possibility that the observed compressive waves are slow (acoustic) waves generated in the corona through the nonlinear dissipation of Alfvén waves that originate in the photosphere. It is also possible that turbulence driven by reflection of Alfvén waves in the corona (e.g., Cranmer 2010) generates compressive waves. In either case the compressive waves should eventually dissipate through shock generation to heat the corona, and we thus suggest that the observations have captured one aspect of coronal heating.

In the analysis above, we considered outgoing slow waves only and the possible contribution of downward waves was ignored based on the theoretical expectation that outgoing slow waves are preferentially generated from outgoing Alfvén waves (Goldstein 1978; Derby 1978; Kudoh & Shibata 1999; Suzuki & Inutsuka 2005, 2006). In the case of downward waves, $(v_{\rm sw} + c_s)$ in Equation (4) is replaced with $(v_{\rm sw} - c_s)$, and the density amplitude would be increased 2–30 times without changing the qualitative feature of the radial variation. On the other hand, the modified energy flux S_c would not be changed because the replacement of $(v_{\rm sw}+c_s)$ by $(v_{\rm sw}-c_s)$ in Equation (6) is canceled out by the change in v'.

Here we should note that a strict quantitative comparison between the observation and the numerical model is difficult because of various uncertainties that are not taken into account. First, only quasi-monochromatic fluctuations are considered as waves in our study, leading to underestimation of the energy flux. If the wave field is a superposition of waves having various periods, apparently random fluctuations would be observed, and thus the spectral power would not exceed the 95% statistical significance level. Second, the possible occurrence of statistically significant peaks outside the spectral range of the wavelet analysis would also lead to underestimation of the energy flux. Third, considering the intermittent nature of wave packets, the energy flux will be overestimated by a factor of 2–3. Fourth, the background electron density can change by a factor of 2–3 depending on the empirical model adopted (see comparison of models in Pätzold et al. 1987). Fifth, the model of Suzuki & Inutsuka (2005) considers heating in coronal holes, while the observations were conducted above the quiet Sun region (Imamura et al. 2014). Sixth, generation of compressive waves tends to be overestimated in one-dimensional models (Suzuki & Inutsuka 2005). Nevertheless, the marked increase of S_c with distance by two orders of magnitude is considered a robust feature, and the conclusions based on this result would not change.

5. CONCLUSIONS

We studied the radial dependence of the characteristics of electron density fluctuations in the corona at 1.5–20.5 R_S by spectral analysis of radio frequency fluctuations measured during the solar conjunction of the *Akatsuki* spacecraft. The power spectra at 3.5–20.5 R_S show near power-law shape close to Kolmogorov over the frequency interval 10^{-3} Hz $< \nu < 10^{-1}$ Hz (periods of 10–1000 s), while those at closer heliocentric distances show prominent bump features (Figure 2). Superposed on this background, quasi-periodic disturbances, which are considered signatures of compressive waves, were detected by wavelet analysis of the frequency time series (Figure 4). The wave period ranges from 100 to 2000 s, and the coherence time, which is a measure of the length of the wave packet, tends to be on the same order of magnitude as the wave period. The amplitude of the fractional density fluctuation increases with radial distance, from 0.1%–1% at 1.5 R_S to $\sim$30% at 5.4 R_S (Figure 7). At farther distances the amplitude shows a tendency to saturate or decrease. The estimated maximum amplitude suggests that nonlinearity of the wave field and the resultant wave breaking are potentially important.

Wave energy fluxes were estimated on the assumption that the observed periodic fluctuations are acoustic waves (Figure 8). A radial increase of the energy flux is clearly observed, suggesting that the waves are generated in the extended corona. It is possible that Alfvén waves originating from the photosphere undergo dissipation in the extended corona through generation of acoustic waves. The waves observed in this study are considered to be the same phenomena as the QPCs studied by Efimov et al. (2010, 2012); we revealed the distinct radial variation of the wave amplitude and the energy flux for the first time.

The method developed in this study can be applied to other existing coronal sounding data obtained using spacecraft. Comparison of wave activities in different coronal regions (holes and quiet-Sun) and different phases of the solar cycle would constrain the physical processes governing the characteristics of acoustic waves. Further observations of Alfvén waves using a Faraday rotation technique are also desirable. By combining the observations of the amplitudes and the energy fluxes of both Alfvén waves and acoustic waves and comparing these with theoretical models, we can greatly improve our understanding of the propagation and dissipation of waves and the resultant coronal heating. The information on turbulence obtained from phase/frequency spectra (Figure 2) and amplitude scintillation spectra (Imamura et al. 2014) would also constrain dissipation processes.

We thank the members of the *Akatsuki* project team, the VLBI group, the UDSC operation team, and the *Hinode* team for supporting the experiment. The ultra-stable oscillator on board the *Akatsuki* spacecraft was manufactured by TimeTech GmbH. We also thank M. K. Bird, T. Suzuki, and T. Matsumoto for making valuable comments on this study. Comments made by the anonymous reviewer greatly improved the paper.

REFERENCES

Andreev, V. E., Efimov, A. I., Samoznaev, L. N., et al. 1997, SoPh, 176, 387
Balasubramaniam, K. S., & Pevtsov, A. A. 2011, Proc. SPIE, 8148, 814809
Carlsson, M., Hansteen, V. H., De Pontieu, B., et al. 2007, PASJ, 59, 663
Chashei, I. V., Bird, M. K., Efimov, A. I., et al. 1999, SoPh, 189, 399
Cranmer, S. R. 2002, SSRv, 101, 229
Cranmer, S. R. 2010, ApJ, 710, 676
De Forest, C. E., & Gurman, J. B. 1998, ApJL, 501, L217
De Pontieu, B., McIntosh, S. W., Carlsson, M., et al. 2007, Sci, 318, 1574
Derby, N. F. 1978, ApJ, 224, 1013
Efimov, A. I., Lukanina, L. A., Samoznaev, L. N., et al. 2010, in AIP Conf. Proc. 1216, Twelfth International Solar Wind Conference, ed. M. Maksimovic et al. (Melville, NY: AIP), 90
Efimov, A. I., Lukanina, L. A., Samoznaev, L. N., et al. 2012, AdSpR, 49, 500
Efimov, A. I., Lukanina, L. A., Rogashkova, A. l., et al. 2013a, J. Commun. Technol. Electron., 58, 901
Efimov, A. I., Lukanina, L. A., Rogashkova, A. I., et al. 2013b, J. Commun. Technol., 58, 429
Erdélyi, R., Malins, C., Tóth, G., & De Pontieu, B. 2007, A&A, 467, 1299
Goldstein, M. L. 1978, ApJ, 219, 700
Gupta, G. R., Teriaca, L., Marsch, E., et al. 2012, A&A, 546, A93
Hollweg, J. V., Bird, M. K., Volland, H., et al. 1982, JGR, 87, 1
Imamura, T., Iwata, T., Yamamoto, Z., et al. 2010, SSRv, 154, 305
Imamura, T., Noguchi, K., Nabatov, A., et al. 2005, A&A, 439, 1165
Imamura, T., Toda, T., Tomiki, A., et al. 2011, EP&S, 63, 493
Imamura, T., Tokumaru, M., Isobe, H., et al. 2014, ApJ, 788, 117
Isobe, H., Proctor, M. R. E., & Weiss, N. O. 2008, ApJ, 679, 57
Jacques, S. A. 1977, ApJ, 215, 942
Jensen, E. A., Nolan, M., Bisi, M. M., et al. 2013, SoPh, 285, 71
Jess, D. B., Mathioudakis, M., Erdélyi, R., et al. 2009, Sci, 323, 1582
Kojima, M., & Kakinuma, T. 1990, SSRv, 53, 173
Kopp, R. A., & Holzer, T. E. 1976, SoPh, 49, 43
Kosugi, T., Matsuzaki, K., Sakao, T., et al. 2007, SoPh, 243, 3
Kudoh, T., & Shibata, K. 1999, ApJ, 514, 493
Matsumoto, T., & Suzuki, T. K. 2012, ApJ, 749, 8
McIntosh, S. W., De Pontieu, B., Carlsson, M., et al. 2011, Natur, 475, 477
Nakamura, M., Imamura, T., Ishii, N., et al. 2011, EP&S, 63, 443
Nemec, A. F., & Nemec, J. M. 1985, AJ, 90, 2317
Ofman, L., Nakariakov, V., & De Forest, C. E. 1999, AJ, 514, 441
Ofman, L., Romoli, M., Poletto, G., et al. 1997, ApJL, 491, L111
Ofman, L., Romoli, M., Poletto, G., et al. 2000, ApJ, 529, 592
Okamoto, T. J., Tsuneta, S., Berger, T. E., et al. 2007, Sci, 318, 1577
Pätzold, M., Bird, M. K., Volland, H., et al. 1987, SoPh, 109, 91
Shiota, D., Tsuneta, S., Ito, H., et al. 2012, in ASP Conf. Ser. 454, Hinode-3: The 3rd Hinode Science Meeting, ed. T. Sekii et al. (San Francisco, CA: ASP), 375
Spangler, S. R. 2002, ApJ, 576, 997
Suzuki, T., & Inutsuka, S. 2005, ApJ, 632, L49
Suzuki, T., & Inutsuka, S. 2006, JGR, 111, A06101
Tomczyk, S., McIntosh, S. W., Keil, S. L., et al. 2007, Sci, 317, 1192
Torrence, C., & Compo, G. P. 1998, BAMS, 79, 61
Woo, R., & Armstrong, J. W. 1979, JGR, 84, 7288
Woo, R., Armstrong, J. W., Bird, M. K., et al. 1995, GeoRL, 22, 329